Citation for final published version:

Sikdar, Shirsendu, Kudela, Pawel, Radzieński, Maciej, Kundu, Abhishek and Ostachowicz, Wiesław 2018. Online detection of barely visible low-speed impact damage in 3D-core sandwich composite structure. Composite Structures 185 , pp. 646-655. 10.1016/j.compstruct.2017.11.067

Publishers page: http://dx.doi.org/10.1016/j.compstruct.2017.11.067

Online Detection of Barely Visible Low-speed Impact Damage in 3D-core Sandwich Composite structure

Shirsendu Sikdar[1], Pawel Kudela[2], Maciej Radzieński[3], Abhishek Kundu[4] and
Wiesław Ostachowicz[5]
Email: ssikdar@imp.gda.pl[1], pk@imp.gda.pl[2], maciej.radzienski@imp.gda.pl[3],
KunduA2@cardiff.ac.uk[4], wieslaw@imp.gda.pl[2]
[1,2,3,5]Institute of Fluid-Flow Machinery, Polish Academy of Sciences, 14, Fiszera Street,
Gdansk 80-231, Poland
[4]Cardiff School of Engineering, Cardiff University, The Parade, Queen's Building, Cardiff,
CF24 3AA, UK.
[5]Warsaw University of Technology, Faculty of Automotive and Construction
Machinery, Narbutta 84, 02-524 Warsaw, Poland

Abstract

3D-core sandwich composites are novel lightweight construction materials being used heavily in defense, aerospace, marine, and automobile industries. In spite of the many commendable advantages, the 3D-core sandwich composite structures are prone to barely visible low-speed impact damages that may significantly jeopardize the safety and integrity of the structural assembly. The aim of this paper is to develop an advanced structural health monitoring framework to efficiently identify such damages in the sandwich structure using ultrasonic guided wave propagation. Theoretical analysis, numerical simulations and laboratory experiments of guided wave propagation in 3DCSCS have been carried out to demonstrate the effectiveness of the identification of barely visible impact damages. It is found that the presence of such damage regions significantly magnifies the fundamental antisymmetric mode of the propagating signals. The 3D numerical simulation gives physical insight and a good agreement has been observed with experimental results which affirms our understanding of the effect of damage on the propagating waves. The impact damage regions in the sandwich structure are experimentally identified using a modified signal difference algorithm based health monitoring framework. The proposed structural monitoring framework is found to be significantly efficient for the detection of impact damages in a sandwich structure.

Keywords: 3D-core sandwich composite structure; guided wave; piezoelectric transducer disc; barely visible impact damage; dispersion; Laser-Doppler-Vibrometer.

1. Introduction

Honeycomb sandwich composites have proven their usefulness as lightweight construction materials due to their high strength-to-weight ratio, effective acoustic damping and high energy-absorption capability [1]. The 3D-core sandwich composite structures (3DCSCS) is one of these sandwich structures, which consist of two thin glass fiber reinforced composite (GFRC) face-sheet (skin) bonded to a relatively thick and lightweight composite hexagonal honeycomb core [2]. The function of the face-sheets is to carry in-plane and bending forces, while the purpose of the core is to keep together the skins and to persuade transverse shear loadings [3]. The combination of thin, stiff skins and thick-core results in a lightweight structure with high load-bearing capacity. However, low-speed foreign object impacts can cause significant localized damage or debondings at the skin-core interphase. These impacts are frequently caused due to improper handling, tools drops, and encounter with runway debris, amongst others [4-7. It should be noted that such type of defects generally are not readily noticeable and can grow due to aging, cyclic loading or due to an intensive load on the structure, which may cause a major loss in stiffness and jeopardize the safety and overall integrity of the structure [8]. Thus, identification of such barely visible or hidden defects is crucial to prevent failures of sandwich structures.

An experimental and analytical impact damage study on a highly loaded sandwich fuselage keel panel made of graphite-epoxy skins and honeycomb core was presented in [9]. It was shown that the low-speed impact defects depend on the impact energy and velocity (low-speed impact was defined as less than 50J in impact energy and 4-8 m/s impact velocity for the studied sandwich structure). Several attempts have been made previously to represent the barely visible low-speed impact damage (BVLID) phenomena and to develop detection techniques to assess different damage types [10-13]. A comparison between different identification methods including visual, shearography and C-scan to inspect the post-impact damages/defects of a sandwich composite structure was presented in [12]. Some authors [11-12] described the study on nonlinear elastic wave spectroscopy to detect BVLIDs in carbon-fiber reinforced composites, based on the influence of dynamic characteristics of composites. An experimental study on impact damage identification in sandwich composite structures using Lamb wave excitation and Laser-Doppler-Vibrometer (LDV) was presented in [10].

The ultrasonic guided wave (GW) based inspection methods have the capability to identify defects in sandwich structures [14-18]. The major referred advantages of the GW based

BVLID inspection methods are the resulting modification in wave packets based on their phase-velocity and frequency, potential to penetrate into the hidden layers and the long distance inspection capability [19-20]. It has also been reported that the proper identification of different wave modes is crucial to the success of GW based non-destructive evaluation (NDE) and structural health monitoring (SHM) of composite structures using piezoelectric actuator/sensors [21]. It is was also stated that the complex nature of sandwich composite structures inherently imposes many challenges for the understanding of GW propagation phenomenon with different excitation frequencies. The GW propagation characteristics in aluminum-skin and hexagonal shaped Nomex-core sandwich structures, using surface-bonded piezoelectric actuator-sensor system was numerically and experimentally investigated in [22]. A significant increment in the propagating GW signal amplitudes due to the presence of debondings in the sandwich structure was observed in several studies [17,18,23]. A debonding detection algorithm for sandwich composite structures, which uses the received GW signals from surface-bonded sensor network as inputs were presented in [14]. An online structural damage identification method based on the constrained dual extended Kalman filter was proposed in [24].

Non-contact laser measurement techniques have also been proposed by many authors [25-27]. The scanning LDV technique allows capturing the full wavefield in the structural elements. The application of scanning LDV for Lamb wave propagation measurements was first introduced in [15]. A more refined damage visualization method based on frequency-wavenumber domain filtering, which uses the incident wave removal procedures was proposed in [26]. Such procedures have the objective of filtering the transducer generated waves to obtain a residual wavefield that comprises only of the contributions of scattered waves. The residual wavefield analysis technique was successfully applied for baseline-free characterization and identification of damage in composite panels [27]. Filtering mask in the wavenumber domain has been proposed as an alternative approach to improve damage localization accuracy [29]. This technique eliminates the boundary reflections obscuring weaker damage reflection and thereby the whole surface can be inspected and analyzed as opposed to the techniques proposed in [26,27,30]. This approach for multiple damage localization as well as size estimation was further enhanced in [20]. In the study, the authors presented the capabilities of the technique for assessment and identification of cracks in composite thin-walled structures by using full wavefield data from out-of-plane velocity components. The effectiveness of the technique was successfully verified by comparing with numerical and experimental results.

A limited number of theoretical studies on wave propagation in sandwich structures have also been reported which investigate the dispersion characteristics and elastic response of the propagating GWs due to transient surface loading [31-34]. More efficient 2D semi-analytical models with limited applications have been developed for GW propagation in sandwich plates [35-37]. Recently, a global matrix method based robust semi-analytical model for rapid calculations of time-dependent transient surface excitation induced elasto-dynamic fields in a laterally unbounded sandwich composite plate was developed [38]. The 2D model has shown its potential to accurately analyze the modal characteristics of propagating GW signals in a triple-layered composite sandwich structure. However, GW propagation and BVLID identification in 3DCSCS has not been studied yet and remains open to investigation.

In this paper, theoretical dispersion curves have been derived for GW propagation in the 3DCSCS in the ultrasonic frequency range. Based on the obtained dispersion curves, different GW modes in the numerically and experimentally obtained sensor signals are identified. A 3D finite element simulation of GW propagation in 3DCSCS with BVLIDs is carried out in ABAQUS. Laboratory experiments are conducted to verify the simulation results, and to identify the BVLIDs. A parametric study is also carried out to study the BVLID size effects on the propagating GW modes. The BVLID induced differential features in the sensor signals are captured by applying an advanced probability based coefficient-of-signal-difference (CSD) algorithm, which uses an image-fusion technique to image the BVLID regions. Further, a full-wavefield measurement based experimental investigation is also carried out to locate the BVLID regions in the 3DCSCS to verify the efficiency of the proposed SHM framework.

2. Experimental setup and selection of operating signal

An experimental setup has been configured to carry out the inspection of 3DCSCS using PTD actuator-sensory network based on GW propagation strategy for the proposed SHM-framework and a separate setup for full wavefield measurement has been made using a single-headed scanning LDV and PTD actuator. The following sub-sections explain both the GW propagation based experimental setups in detail.

2.1. Sample 3DCSCS plate and experimental setup for the proposed SHM-framework

A hexagonal shaped epoxy honeycomb foam core (3D-core) and GFRC-skin made 3DCSCS (500 mm × 500 mm × 7 mm) sample plate is selected for the laboratory experiment,

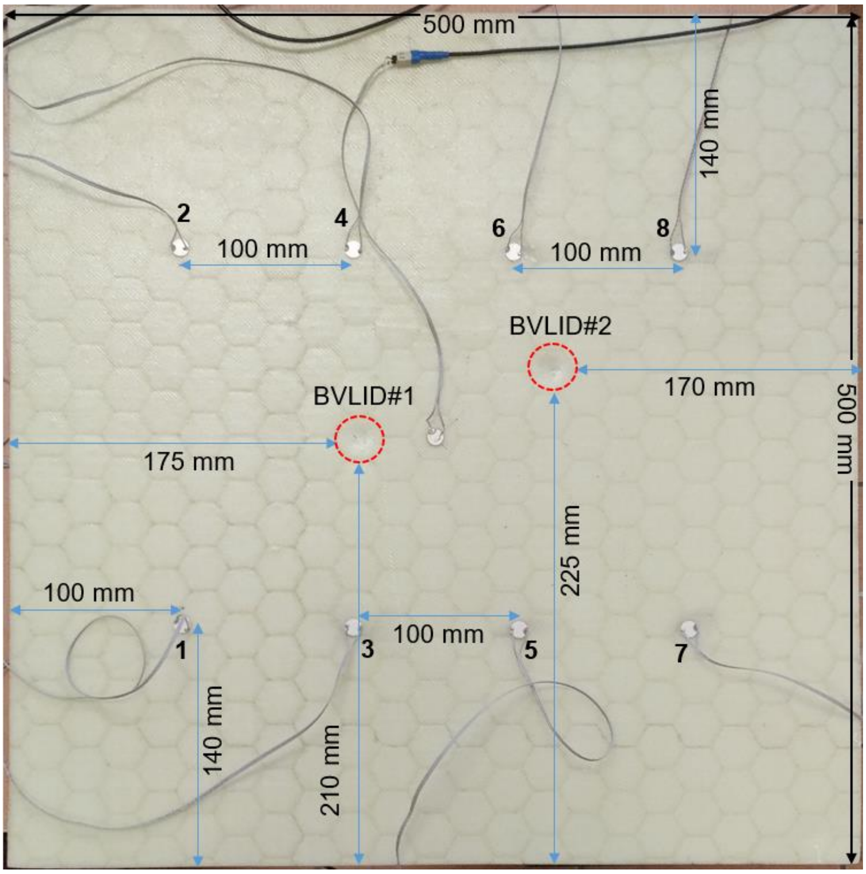

Fig 1: Experimental sample 3DCSCS plate with BVLIDs.

as shown in Fig. 1. The layer-wise elastic material properties of the 3DCSCS are shown in Table 1. In the sample plate, two BVLID regions are introduced at different locations by using

Table 1. 3DCSCS elastic material properties.

Material	E_1 (GPa)	E_2 (GPa)	E_3 (GPa)	G_{12} (GPa)	G_{23} (GPa)	G_{13} (GPa)	ν_{12}	ν_{13}	ν_{23}	ρ (kg/m^3)	t (mm)
GFRP-skin	30.35	30.35	5.9	12.42	3.66	3.66	0.05	0.26	0.26	2400	0.98
3D-core	1.45	1.45	2.33	0.088	0.172	0.172	0.42	0.42	0.42	78	5
Adhesive	0.0486	0.0486	0.0486	0.0174	0.0174	0.0174	0.40	0.40	0.40	1110	0.02

a standard low-speed steel ball-drop impact device with an impact energy of 10 J, as shown in

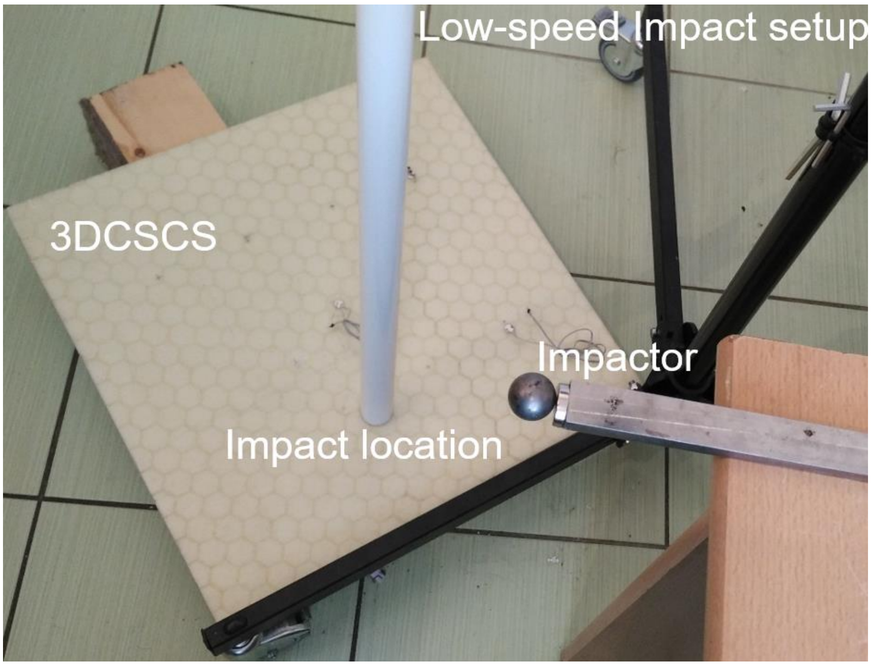

Fig. 2. Experimental setup for the low-speed impact on the 3DCSS.

Fig. 2. The visual effect of the impacted regions appears to be circular in shape with approximately 15 mm in diameter. In the setup, circular PTDs (NCE51) of 10 mm diameter and 0.4 mm thickness are applied for both actuation and reception of GW signals in the 3DCSCS.

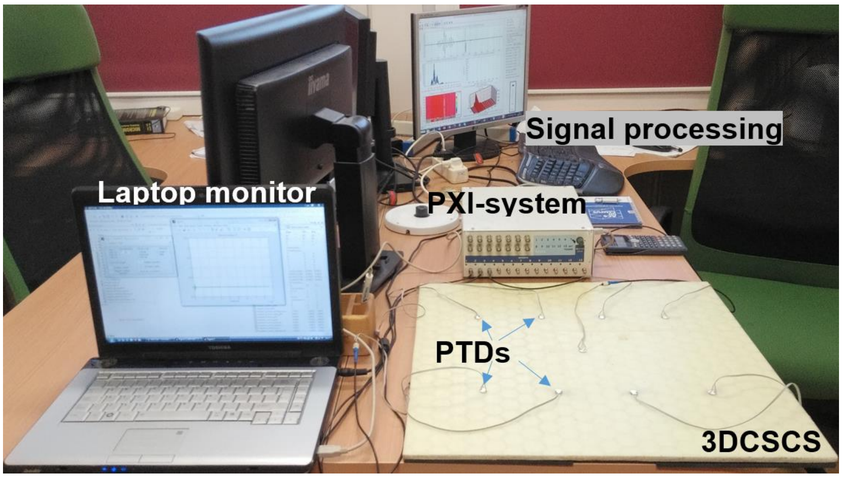

Fig. 3. Experimental setup for the GW based SHM of 3DCSS using PTDs.

In order to operate the PTDs, the setup is configured with a multi-channel function-generator (FGEN) cum data-acquisition (DAQ) based PXI-system, a computer to control the

PXI-system and to save the required sensor data. The complete experimental setup is shown in Fig. 3.

2.2. Selection of operating signal for the PTDs

An optimum operating frequency of the PTDs is determined by placing two PTDs (actuator-sensor) on the sample plate at a distance of 220 mm, as shown in Fig. 4(a). In this process, a predefined range of actuator frequencies are applied and the corresponding sensor signals are collected. The collected signals are then analyzed to calculate maximum responses for different actuation frequencies and a frequency-response plot is generated, as shown in Fig. 4(b). It is found that the PTDs are showing highest A0-mode response around 100 kHz frequency. Thus, a 100 kHz 5-cycle sine Hanning pulse represented in Fig. 5 is selected as actuation frequency for all the cases unless stated otherwise.

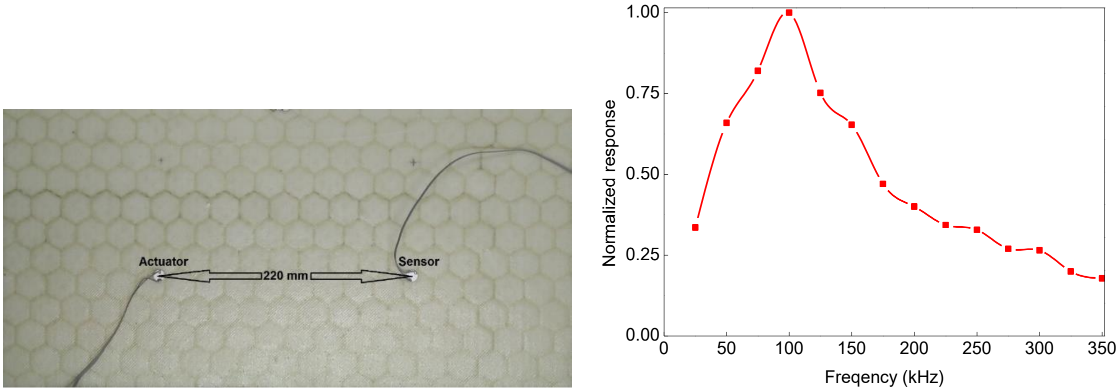

(a) (b)

Fig. 4. (a) Setup for driving frequency optimization of PTDs and (b) corresponding calibration curve for frequency modulation.

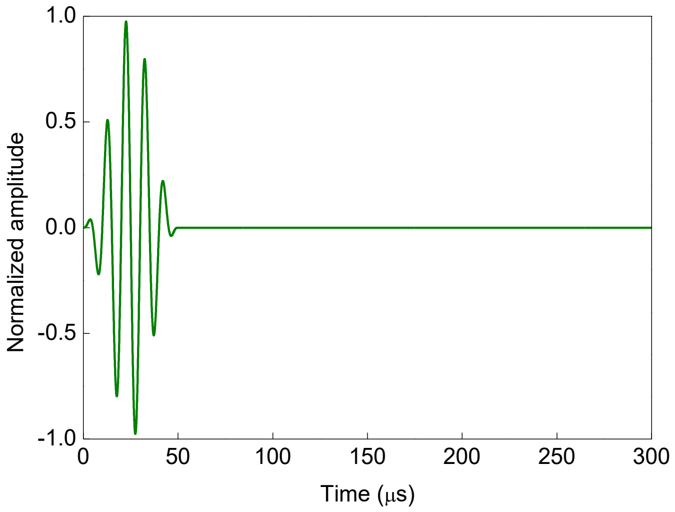

Fig. 5. 100 kHz 5-cycle Hanning input pulse.

2.3. Experimental setup for wavenumber domain signal processing using LDV

In order to identify the BVLID effects, a single-headed scanning LDV (Polytec PSV-400) is applied for the full-wavefield measurement of a PTD-actuated propagating GWs in the sample 3DCSCS. The scanned wave data obtained from predefined grid points on the sample plate is registered in the form of out-of-plane velocities. A schema of the experimental setup for LDV test is presented in Fig. 6. In the setup, an actuator-PTD was mounted at the center of the sample plate to generate the GWs. An arbitrary waveform-generator and an amplifier are used to generate user-defined excitations in the form of a Hanning window modulated 5-cycle tone-burst sinusoidal signals with carrier-frequency of 10 kHz and 15 kHz respectively. A scanning-head which is connected to a DAQ and a controller is aligned such a way that the laser-beam is normal to the surface of the target-specimen and orients its scanning mirror to set an appropriate decoder to provide a voltage-proportional to the registered velocity. These measured velocities are obtained from the Doppler-shift which is a frequency shift in the reflected laser signal caused by movement in the scanned sample plate. The digital generator is connected to a controller by a synchronization cable. Initially, the elastic-waves are generated and registered synchronously in one point of the grid on the sample plate surface, in order to set up the wave attenuation time. The waves are then re-generated from the actuator-PTD but the laser-beam measures velocities in the next grid point.

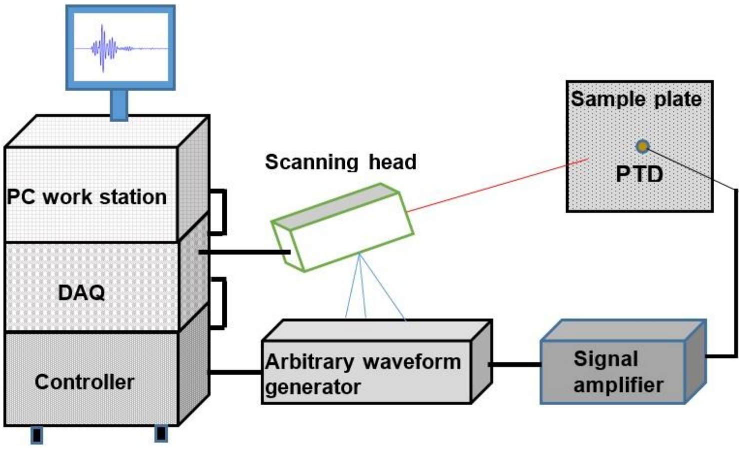

Fig. 6. Schema of the experimental setup for scanning LDV test on the 3DCSCS

3. Numerical Simulation

Analytical prediction of BVLID effects on the propagating GWs in 3DCSCS with BVLIDs is difficult, owing to the complexities involved in the structural geometry and the boundary conditions. Hence, the BVLID effects on the propagating GWs are numerically analyzed using the finite element simulation in ABAQUS.

Towards this, 3D numerical modeling of GW propagation in a 3DCSCS is carried out using a surface-bonded PTD actuator-sensor network, in accordance with the experiments to be conducted in the laboratory. The numerical simulation of PTD induced GW propagation in 3DCSCS is challenging, as both the implicit and explicit time-stepping algorithms are required for the transient dynamic analysis. This is because only the implicit solver is not sufficient to accurately handle the simulation of wave propagation. Moreover, the piezoelectric elements are not available in the explicit code but it is available in the implicit code in ABAQUS [31]. Therefore, the 3DCSCS (500 mm × 500 mm× 7 mm) plate is modeled using the explicit code and the PTDs (10 mm diameter and 0.4 mm thin) are modeled using the implicit code. The ABAQUS 'standard explicit co-simulation technique' is applied to correlate the explicit and the implicit analysis of GW propagation in the 3DCSCS [39].

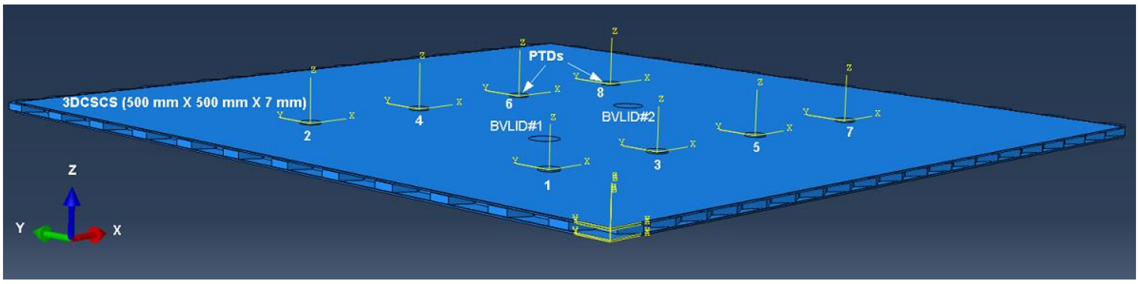

Fig. 7. Numerical model of experimental 3DCSCS.

In the explicit modeling of 3DCSCS, the 8-noded C3D8R linear brick elements (hourglass control and reduced integration) are used. In order to model the BVLIDs, two zero-volume circular BVLID regions (BVLID#1 and BVLID#2) with 15 mm diameter are modeled by de-merging element nodes (resembling debonding) at the adhesive-skin and core-adhesive interphase, as shown in Fig. 7. The layer-wise element sizes are considered as: 3D-core: 0.5 mm × 0.5 mm × 0.25 mm, GFRC-skin: 0.5 mm × 0.5 mm × 0.245 mm and adhesive: 0.5 mm × 0.5 mm × 0.01 mm. Whereas, in the implicit modeling of PTDs (actuator/sensor), the 8-noded standard C3D8E linear piezoelectric brick element with six degrees of freedoms (DOF) at each node is considered. The C3D8E elements have the potential to capture the electromechanical coupling mechanism of the PTDs, where the electrical voltage is assigned as the additional DOF in the coupling element. The selected user-defined input signal (voltage) is applied to the top-surface nodes of the actuator-PTDs, and zero voltage is assigned to the bottom-surface nodes of the actuator as well as sensor-PTDs to carry out the grounding operation. On the contrary, the output signal (voltage) is recorded at the top surface of the sensor-PTDs. In the numerical simulation, the NCE51 PTD material properties are assumed based on the manufacturer's information as:

$$[e]=\begin{bmatrix} 0 & 0 & 0 & 0 & 13.7 & 0 \\ 0 & 0 & 0 & 13.7 & 0 & 0 \\ -6.06 & -6.06 & 17.2 & 0 & 0 & 0 \end{bmatrix} \mathrm{C/m^2},$$

$$[\varepsilon]=\begin{bmatrix} 1.72 & 0 & 0 \\ & 1.72 & 0 \\ & \mathit{Symmetry} & 1.68 \end{bmatrix} \times 10^{-8}\, C/Vm,$$

$$[c]=\begin{bmatrix} 13.4 & 8.89 & 9.09 & 0 & 0 & 0 \\ & 13.4 & 9.09 & 0 & 0 & 0 \\ & & 12.1 & 0 & 0 & 0 \\ & & & 2.05 & 0 & 0 \\ & & & & 2.05 & 0 \\ & & \mathit{Symmetry} & & & 2.24 \end{bmatrix} \times 10^{10}\, N/m^2$$

where [*e*] is the piezoelectric stress matrix, [*ε*] is the piezoelectric permittivity matrix and [*c*] represents the mechanical stiffness tensor. The density (ρ) of the piezoelectric material is assumed to be 7750 kg/m^3. The numerical simulation is further broadened for the GW propagation in the 3DCSCS with a range of BVLID sizes, in order to study the influence of BVLID size on the propagating GW signals.

4. Theoretical dispersion curve

A global matrix method based 2D semi-analytical formulation is used to obtain the theoretical frequency versus group velocity dispersion curve for the 3DCSCS, which has proven its potential to accurately determine the dispersion characteristics of propagating GWs in a different type of sandwich composite structures. Detailed formulation of the 2D semi-analytical model for wave field calculations in a multi-layered honeycomb composite sandwich structure can be found in [38] and hence, the formulation will not be repeated here for brevity. The formulation for a triple-layered honeycomb composite sandwich structure was ultimately summarized in a global matrix form as:

$$\begin{bmatrix} \hat{Q}^1 & 0 & 0 \\ Q^1 & -Q^2 & 0 \\ 0 & Q'^2 & -Q^3 \\ 0 & 0 & \hat{Q}^3 \end{bmatrix}_{12\text{x}12} \begin{bmatrix} A^1 \\ A^2 \\ A^3 \end{bmatrix}_{12\text{x}1} = \begin{bmatrix} \vec{F} \\ 0 \\ 0 \\ 0 \end{bmatrix}_{12\text{x}1} \qquad (1)$$

where the Q-matrix (12 × 12) is the global matrix obtained from a complex matrix formulation, the A-matrix (12 × 1) is the constant matrix and the F-matrix (12 × 1) is the excitation matrix. In order to plot the phase-velocity dispersion curves, the dispersion condition can be obtained from the solution of the determinant of the global matrix as:

$$G(\xi_1, \omega) = 0 \tag{2}$$

The values of wavenumber, ξ_1, can be determined for a range of values of frequency, ω, and the corresponding phase-velocity dispersion plots can be obtained by using

$$c_p = \frac{\omega}{\xi_1} \tag{3}$$

where c_p represent the phase-velocity of the guided Lamb wave modes.

It should be noted that the propagating GWs in the plate are represented only by the real-roots of ξ_1. Whereas, the non-propagating wave modes that decay exponentially with propagation distance from the source are represented by the complex-roots of ξ_1.

5. Results and discussion

5.1. Dispersion curve and identification of GW modes

In order to understand the dispersion phenomenon of propagating GWs in the 3DCSCS, the theoretical (Th.) dispersion curve (frequency versus group-velocity) is obtained using the real values of ξ_1 from equation (3) and demonstrated in Fig. 8. The theoretically obtained group velocities are then compared with the numerical (Nu.) and experimental (Ex.) group velocities at different actuation frequencies (50 kHz, 75 kHz, 100 kHz, 125 kHz, 150 kHz, and 200 kHz). From the simulation and experiment, the healthy GW signals are recorded from the PTD at a distance of 220 mm distant (Δx) PTD path#1-2 (actuator-sensor) and the time difference (Δt) between the peak of each envelope of a wave-group or wave-mode at both the reception points (PTD#1 and PTD#2) are determined. Once the time shift (Δt) for the different wave modes is determined, the corresponding group velocity (c_g) can be determined as $c_g = \frac{\Delta x}{\Delta t}$, by employing a TOF analysis as referred in [17]. The group velocities of the experimental signals are represented with symbols on the theoretical dispersion curve, and a substantially good agreement is noticed between the experimental and theoretical group velocities (Fig. 8).

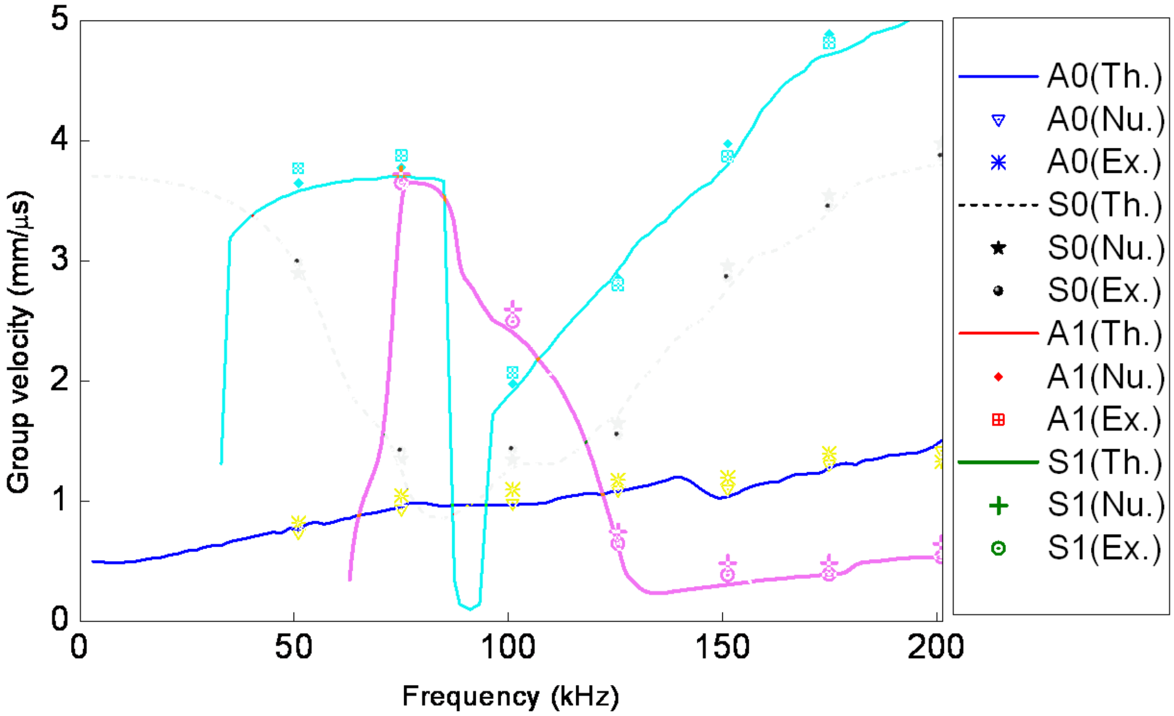

Fig. 8. Group velocity dispersion curve for the 3DCSCS.

It is clearly visible from the plots that the GW propagation in 3DCSCS is multi-modal in nature and there are four individual propagating wave modes at 100 kHz frequency. The anti-symmetric (A) and symmetric (S) wave modes are designated as A0, S0, A1, and S1 (Fig. 8).

5.2. Numerical and experimental study of GW propagation in the 3DCSCS

The finite element simulation in ABAQUS also clearly indicates that the GW propagation in 3DCSCS is multi-modal in nature, as shown in Fig. 9. The generation of multiple independent wave modes corresponding to in-plane displacement is shown in Fig. 9(a) and the propagation of multiple wave modes corresponding to out-of-plane displacement is shown in Fig. 9(b), due to the actuation of PTD#3 with the 5 cycle Hanning input pulse.

Based on the dispersion characteristics in the Fig. 8, the presence of different wave modes (A0, S0, A1, and S1) are identified in the healthy simulated signal (Fig. 10(a)). The simulated signal (surface displacement) corresponding to the actuator-sensor path#1-2 (ref. Fig. 7) is considered as the healthy signal since this path is sufficiently away from the BVLID regions.

In order to clearly understand the characteristics of different wave modes in the healthy numerical signal in frequency domain, the Wavelet transform (WT) is performed on the signal in Fig. 10(a) by using the standard 3D *AGU-Vallen Wavelet window* and presented in Fig.

10(b). The WT coefficient magnitudes at 100 kHz frequency distinctly represent the characteristics of the four individual wave modes in the signal.

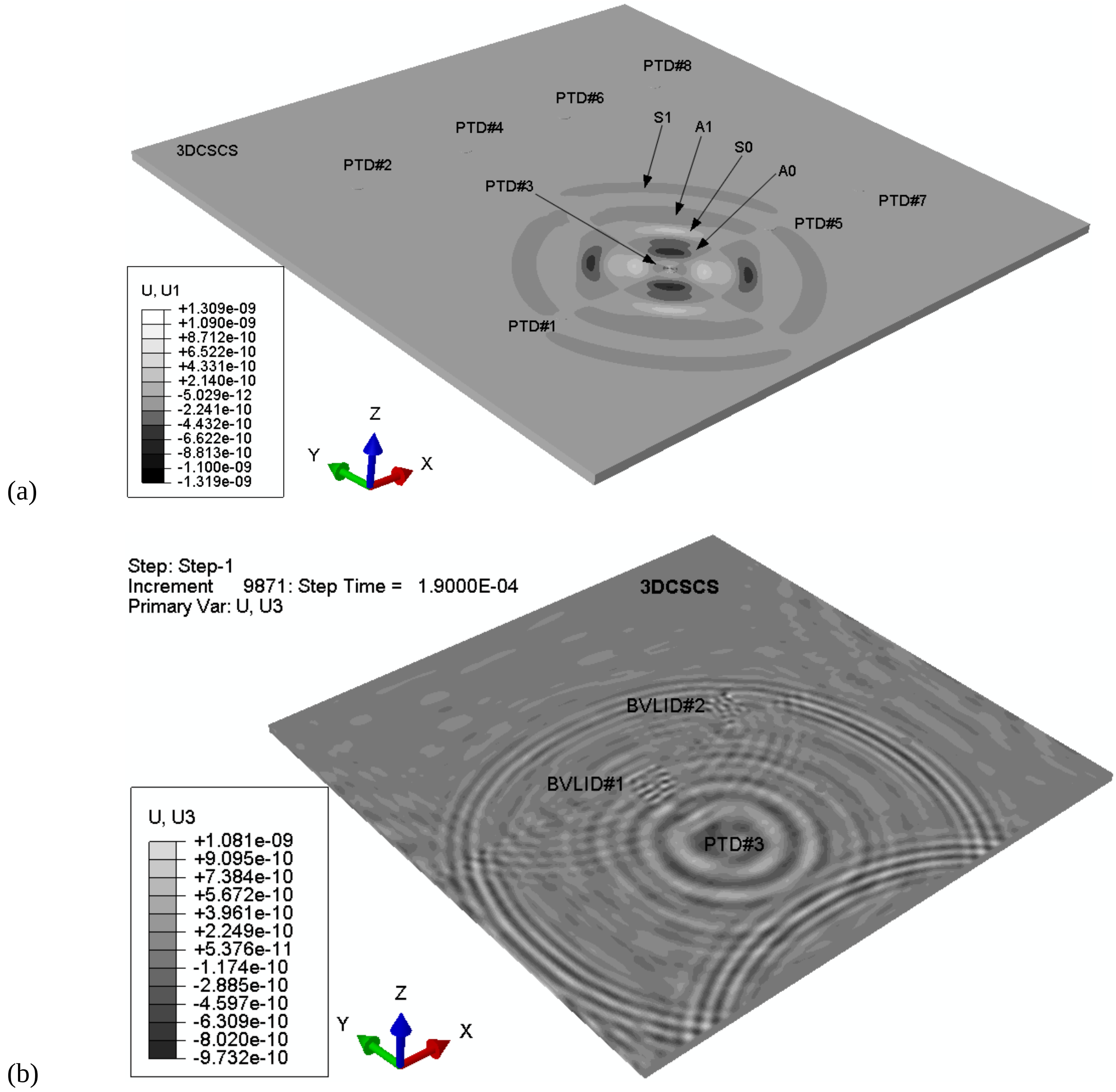

Fig. 9. PTD#3 induced GW propagation in the 3DCSCS model showing the (a) generation of multiple

The BVLID-influenced signal is also collected from the actuator-sensor path#3-4, which is across the BVLID#1. The BVLID signal is then compared with the healthy signal and the comparison shows a significant amplification of the fundamental anti-symmetric (A0) mode in the BVLID signal, as shown in Fig. 11. The major amplification in A0 mode amplitude may be happened due to the considerably lower propagation velocity and a less dispersion and attenuation in comparison with the other wave modes (S0, A1, S1) in the signal at 100 kHz frequency. Moreover, the propagation of primary anti-symmetric mode is highly sensitive to the presence of discontinuities along the thickness direction (out-of-plane).

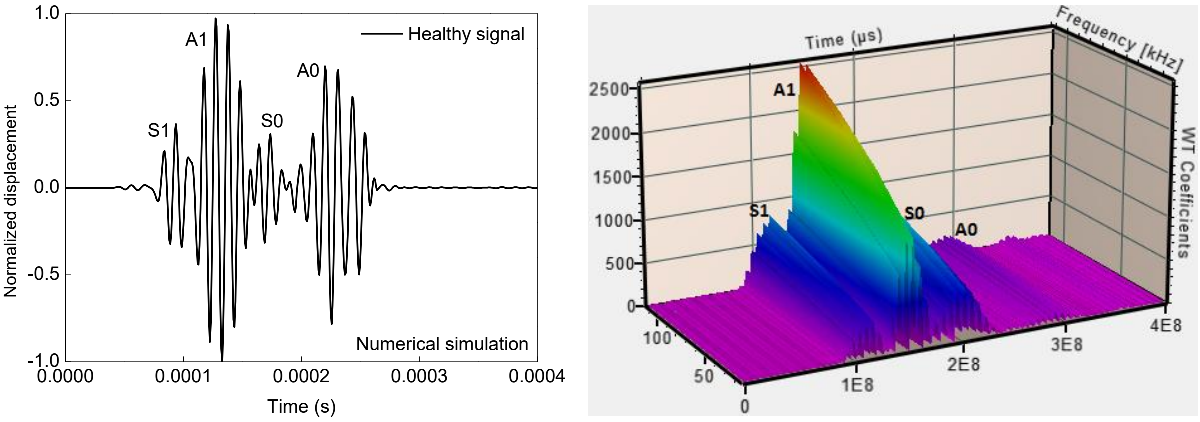

(a) (b)

Fig. 10. (a) Numerical received signal at a 220 mm distant sensor (path#1-2) on the 3DCSCS, (b) 3D representation of the healthy numerical signal in AGU-Vallen Wavelet window.

Similarly, the experimental healthy signal (surface displacement) from PTD path#1-2 (ref. Fig. 1) is obtained from the laboratory experiment and compared with the healthy numerical signal, as shown in Fig. 12. The comparison shows a good agreement between the numerical simulation and the laboratory experiment. The experimental BVLID-influenced sensor signal

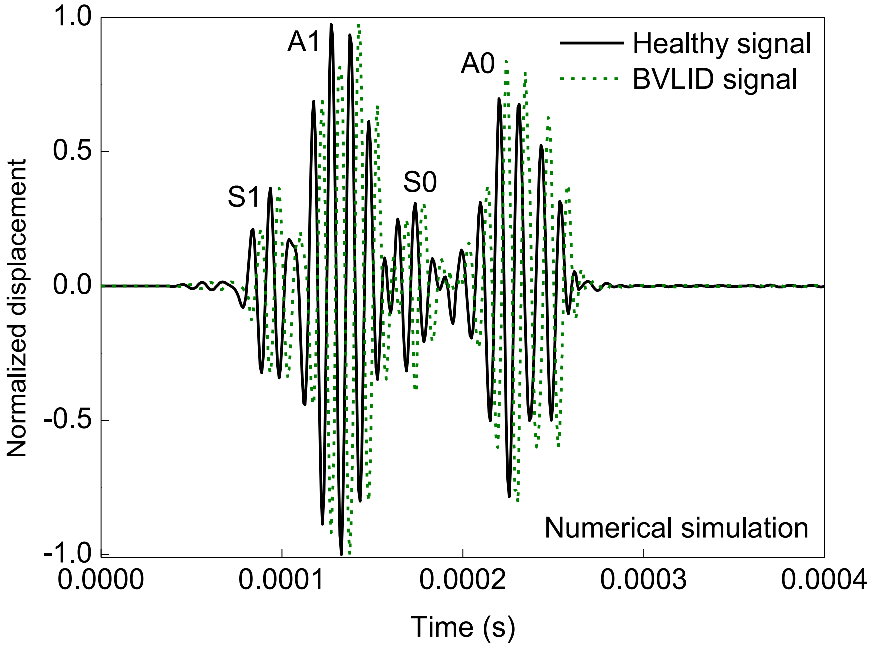

Fig. 11. Comparison of healthy and BVLID sensor signals from numerical simulation.

is then captured from the actuator-sensor path#3-4, which is across the BVLID#1 in the sample 3DCSCS plate (ref. Figure 1). The comparison between the experimental healthy

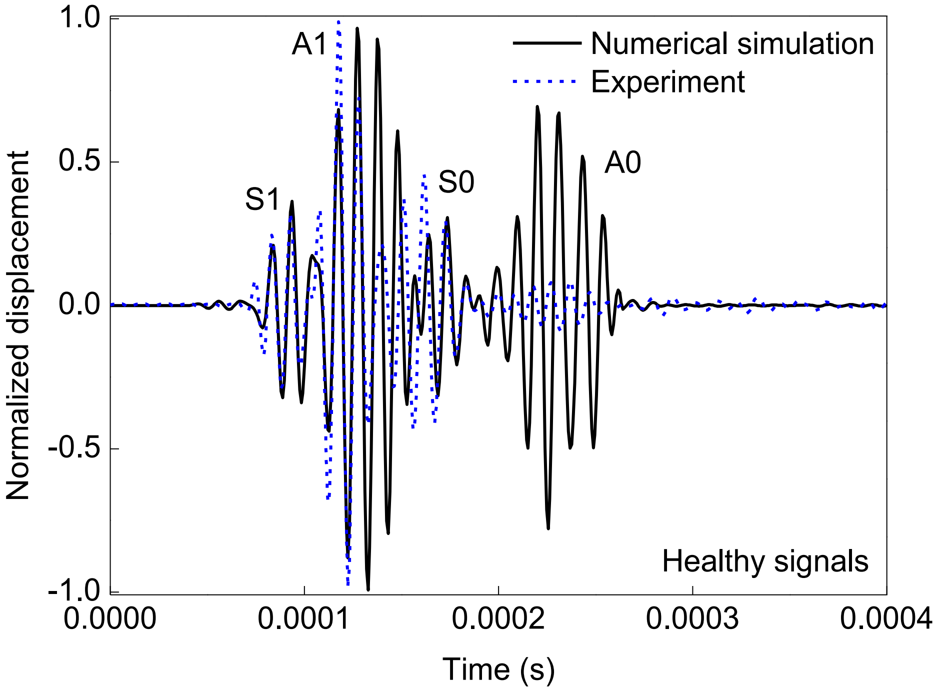

Fig. 12. Comparison of numerical and experimental healthy time-history responses

and BVLID signal is shown in Fig. 13(a), which implies that the presence of BVLID in the 3DCSCS significantly influences the propagating GW signals, in terms of amplification of the A0 mode. The Hilbert transform (HT) of the experimental signals in the Fig. 13(a) is presented

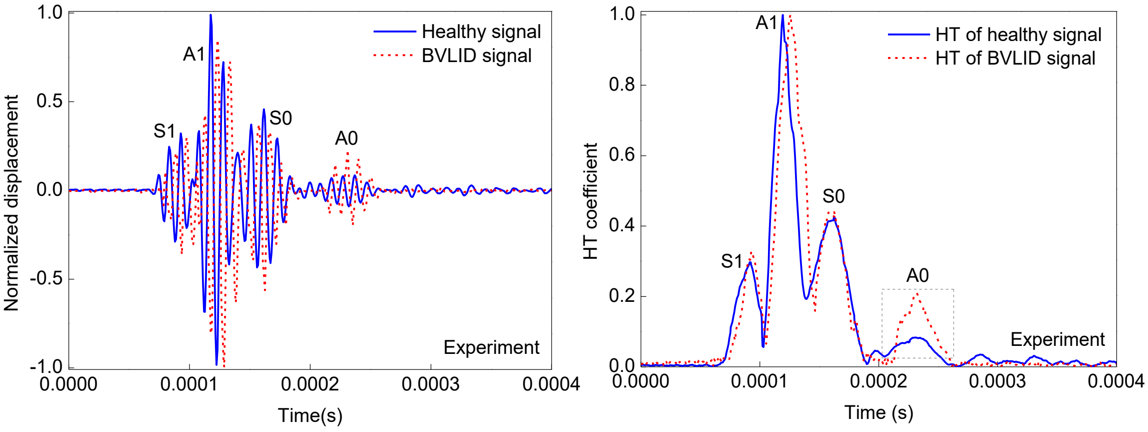

(a) (b)

Fig. 13. (a) Comparison of healthy and BVLID sensor signals from laboratory experiment, (b) Hilbert transform (HT) of experimental time-history responses for healthy and BVLID cases.

in Fig. 13(b), which clearly represents a notable BVLID effect on the A0-mode amplitude. The modal group velocities along different propagation direction are also checked and the results for the A0 mode is presented in Fig. 14. No significant changes in the modal group velocity were observed from GW propagation along the different direction in the 3DCSCS (Fig. 14) which may due to the dominating twill GFRC face-sheet and due to the presence of a certain degree of homogeneity in the core.

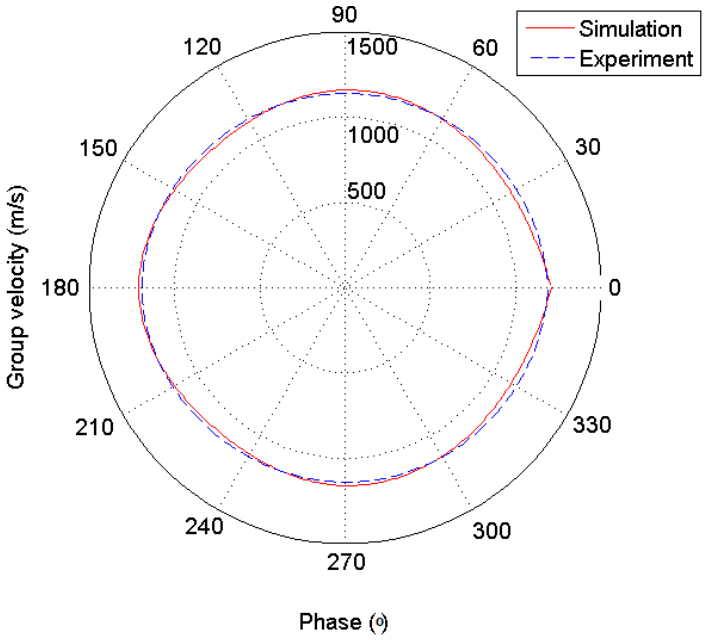

Fig. 14. Directional group velocities of A0 mode in the 3DCSCS at 100 kHz frequency.

5.3. Sensitivity analysis of the BVLID effect

A sensitivity analysis is carried out numerically for a range of BVLID sizes (diameter: 0 mm, 15 mm, 17 mm, 19 mm, 21 mm, 23 mm and 25 mm) to further investigate the BVLID influence on the A0 mode amplitude in the GW signal, and the numerical results are also compared with the possible experimental results (Fig. 15). It is noticed that the increase in BVLID size leads to the increment in A0-mode amplitude, and a good agreement is observed between the numerical and the available experimental results. The increment in modal amplitude may have happened due to the lesser damping across the thickness, as in case of the BVLID region the wave mainly passes through the skin with comparatively higher energy and lesser damping. There is also a possibility of influence due to complex mode-conversion/reflection phenomenon at the BVLID region.

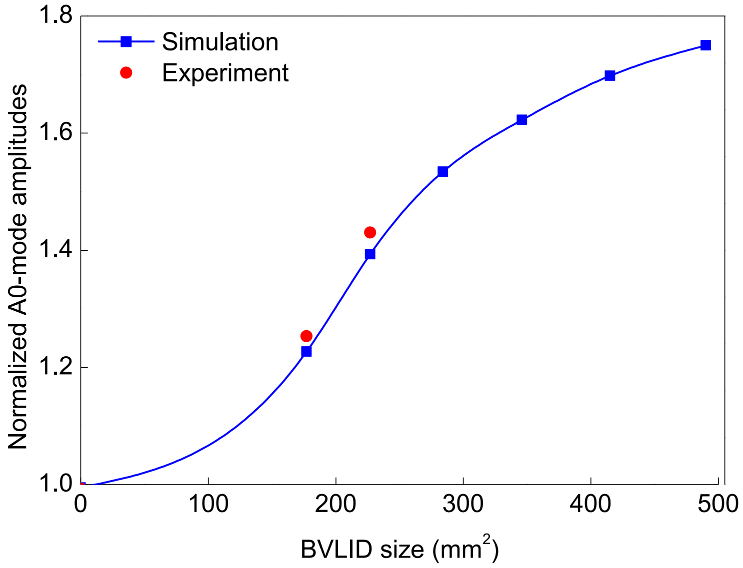

Fig. 15. BVLID size effect on the A0 mode amplitude in the propagating GW signals.

5.4. Identification of BVLID regions in the 3DCSCS

5.4.1. Identification of BVLIDs using CSD algorithm based SHM framework

A CSD algorithm is applied to identify the unknown BVLID regions in the 3DCSCS. The HT of the experimental output signals in the time domain (e.g. Fig. 13(b)) are used for characterization of BVLID influences on the wave modes in the propagating GW signals. In order to capture the differential characteristics of BVLIDs, the CSDs are obtained by comparing the A0-mode amplitudes of the transformed time domain sensor signals. The BVLID probability distribution is computed to visualize the possible defect regions by applying the extracted CSDs as input at each pixel. The image quality is further improved by using an image-fusion technique. The BVLID localization indicator, L_d of any arbitrary position *(x, y)* within the actuator-sensor network can be described as [40]-

$$L_d(x,y)=\sum_{i=1}^{N-1}\sum_{j=i+1}^{N}B_{ij}(x,y)=\sum_{i=1}^{N-1}\sum_{j=i+1}^{N}C_{ij}(x,y)\left[\frac{\psi-R_{ij}(x,y)}{\psi-1}\right] \qquad (4)$$

where, $B_{ij}(x,y)$ is the BVLID distribution probability, measured from the actuator-sensor pair: *i-j* and $C_{ij}(x,y)$ represents the signal difference coefficient, which is the difference in amplitude area between signals with BVLID and without BVLID (healthy) for a particular mode. The CSD is expressed as:

$$C_{ij} = \sqrt{\frac{\int_{t_1}^{t_2} (s^b - s^h)dt}{\int_{t_1}^{t_2} [s^b]^2 dt}} \tag{5}$$

where, s^b and s^h represent the signals with and without BVLID, t_1 is the time of arrival of A0 mode in the signal and t_2= (t_1+ temporal duration of the A0 mode), $\left[\frac{\psi - R_{ij}(x,y)}{\psi - 1}\right]$ is an elliptical contour-shaped spatial distribution function with non-negative values, where

$$R_{ij}(x,y) = \begin{cases} D_{ij}(x,y), & D_{ij}(x,y) < \psi \\ \psi, & D_{ij}(x,y) \geq \psi \end{cases} \tag{6}$$

where,

$$D_{ij}(x,y) = \frac{(\sqrt{(x-x_i)^2 + (y-y_i)^2} + \sqrt{(x-x_j)^2 + (y-y_j)^2})}{d_{ij}} \tag{7}$$

where, d_{ij} represents the distance between transmitter ‘*i*’ and sensor ‘*j*’, and ψ is the scaling parameter, which reduces the size of the BVLID region and it is independent of propagating GW velocity. The magnitude of ψ is obtained empirically and in this study, it is assumed as 1.05 [40].

Based on the change in A0-mode amplitude due to the presence of BVLIDs, the CSD algorithm is applied to interrogate the unknown BVLID regions in the 3DCSCS, using MATLAB. The algorithm uses the HT of the sensor signals (e.g. Fig. 13(b)) collected experimentally from the PTD actuator-sensor network (ref. Fig. 1). The value of BVLID index (CSD magnitudes) at each pixel is determined by processing the sensor signals from the PTD path: 1-2, 3-4, 5-6, 7-8, 1-6, 2-5, 3-8, 4-7, and plotted in Fig. 16(a). The CSD map in Fig. 16(a) clearly represents the actual BVLID regions in the experimental 3DCSCS plate, corresponding to the higher CSD magnitudes. A 3D representation of the CSD map is shown in Fig. 16(b), which distinctly express the influence of BVLIDs on the CSD magnitudes.

5.4.2. Identification of BVLIDs using scanning LDV

This section is dedicated to the identification of BVLID regions in the 3DCSCS using a wavenumber-filtering algorithm, based on the out-of-plane displacement data acquired using the scanning LDV. The key element of the technique is a digital fingerprint of propagating wave in the target-structure captured by a filtering mask. The detailed formulation of the wavenumber-filtering algorithm can be found in [25] for which the excitation and registration of GWs are performed at a rectangular grid of points covering the inspected area on the plate surface. The selected registered 2D data set of propagating waves at an equally sampled time steps can be considered as is in the form of wavefield image. Transformation of each obtained wavefield image from spatial-domain (x,y) to wavenumber-domain (K_x,K_y) is then carried out using the 2D discrete Fourier transform

$$w_n(\mathrm{K}_x,\mathrm{K}_y)=\mathrm{F}_{2D}\left\{w_{x,y,n}\right\} \tag{8}$$

$$\tilde{w}_{x,y,n}=F_{2D}^{-1}\left\{\tilde{w}_n(\mathrm{K}_x,\mathrm{K}_y)\right\} \tag{9}$$

In the formulation, all filtered images are combined by considering the energy dissipation and energy spread in the propagating signals through the 3DCSCS. For measurements with N number of time samples and finite number of measurement points, the energy-based root mean square index (ERMS) can be introduced at the point defined by coordinates x and y as-

$$ERMS_{\mathrm{x,y}}=\sqrt{\frac{1}{N}\sum_{n=1}^{N}\left(\frac{w_{x,y,n}\sqrt{P_n}}{E_n}\right)^2} \tag{10}$$

where $\tilde{w}_{x,y,n}$ is filtered wavefield image in the spatial domain, $E_n=\sum_{x=1}^{Nx}\sum_{y=1}^{Ny}w_{x,y,n}^2$ is the registered normalized discrete GW signal energy at a particular time sample n, P_n is the propagating elastic wave perimeter for an anisotropic plate-like structure, which can be approximated as-

$$P_n\approx\pi\left[\frac{3}{2}(\mathrm{A}_n+B_n)-\sqrt{A_nB_n}\right]=\pi t_n\left[\frac{3}{2}(\mathrm{V}_H+V_V)-(\sqrt{\mathrm{V}_H V_V})\right] \tag{11}$$

where A_n and B_n are the distances traveled by the GWs in in the 3DCSCS along horizontal and vertical direction, respectively. V_H and V_V are A0 mode velocities along horizontal and vertical directions.

The ERMS is used as damage index and can be shown in the form of BVLID influence maps. Any GW disturbances due to the presence of BVLIDs appear as outliers in wavenumber domain outside of the filtering mask. The method presented has been applied to the experimentally obtained data without any additional processing.

The specimen was placed on 50 mm thick polyurethane foam to reduce any external vibration and to ensure uniform support. The measurements were made in 321×321 equally spaced grid points covering whole specimen surface and were made from the opposite side with respect to the actuator. The damage index maps in Fig. 17 clearly show the location of BVLID regions in the sample 3DCSCS with good agreement with the proposed SHM-framework. Thus the LDV based damage metric is used in this paper as a benchmark and for validation of the identified damage location using the improved CSD algorithm discussed earlier. The good agreement highlights the applicability and accuracy of the latter based on GW signal measurements using PDT actuator-sensor network.

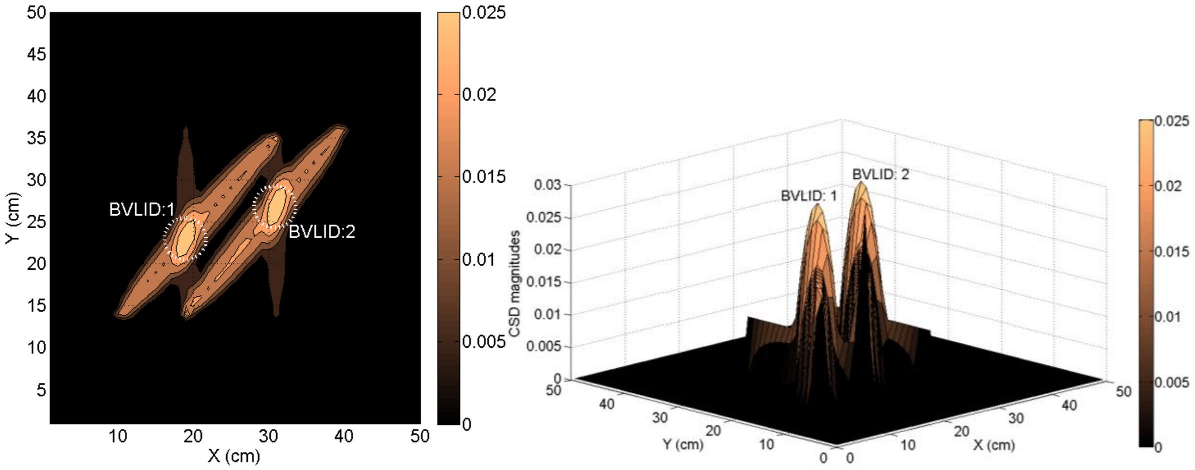

(a)

(b)

Fig. 16. (a) CSD map represents the exact location of BVLIDs, (b) 3D CSD map showing the BVLID effects on the CSD magnitudes.

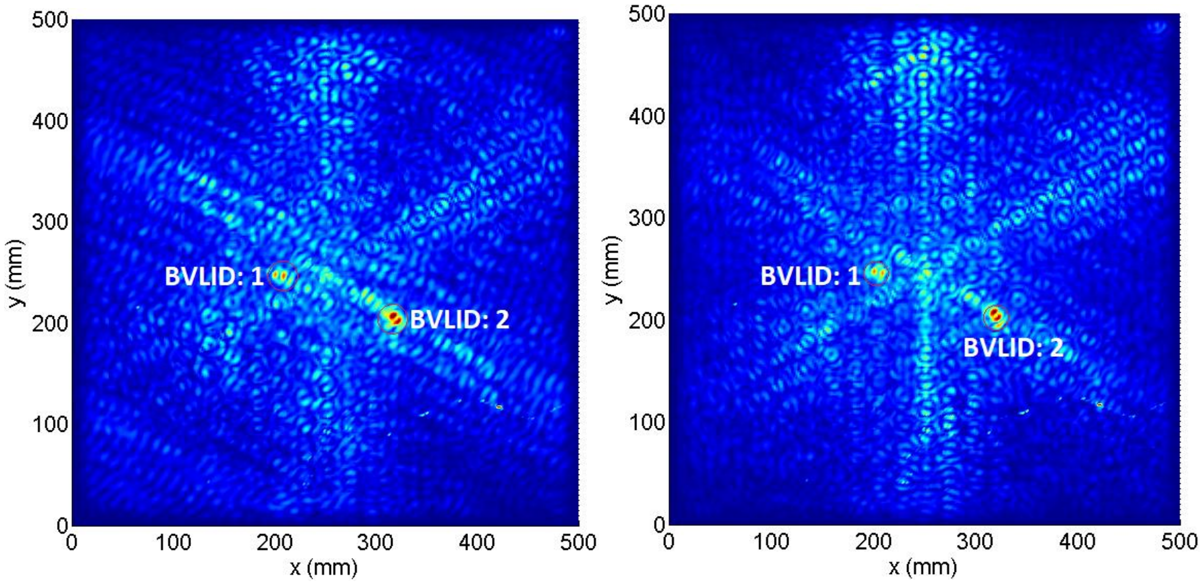

(a)

(b)

Fig. 17. Scanning LDV test obtained damage index maps for (a) 10 kHz and (b) 15 kHz input frequency, respectively.

6. Concluding remarks

Dispersion of the propagating GWs in the 3DCSCS is multi-modal in nature with the presence of four independent wave modes (A0, S0, A1, and S1) at 100 kHz frequency. It is observed that the presence of BVLIDs in the structure significantly amplifies the fundamental anti-symmetric (A0) mode amongst the four wave modes in the GW signals. A good agreement is found between the theoretical, numerical, and experimental results in all the cases that have been studied here. The sensitivity analysis results have shown that the increase in BVLID size leads to an increase in the A0-mode mode amplitude. The proposed CSD algorithm based SHM-framework which works on the basis of change in modal amplitude of the experimental sensor signals has been demonstrated to efficiently localize the BVLID regions in the 3DCSCS within an organized actuator-sensor network of PTDs. From the comparison with LDV based analysis results, it can be clearly stated that the proposed SHM-framework has the potential to more easily and accurately identify the BVLID regions in the 3DCSCS. The proposed framework can be implemented as a robust SHM-framework for online monitoring of different type of sandwich composites, as it relies only on the real-time experimental signal data and this paper is a proof of such implementation. However, it is expected that the baseline signal data can improve the inspection capability of this framework, and the application of this framework is limited to multilayered composite structures with limited wave attenuation and the inspection area is limited to the region inside the sensor-network, which can make this SHM-strategy more viable for practical industrial usage. The future research would involve the development of baseline free algorithms and the detection of delamination and debondings in composite panels using the developed SHM strategy.

Acknowledgements

The research work has been supported by the Polish National Science Centre under grant agreement number UMO-2012/06/M/ST8/00414. SS acknowledges the support from the Polish National Science Centre under grant agreement no UMO-2016/23/N/ST8/01326. AK acknowledges the support from Sêr Cymru, NRN, Wales under grant agreement no NRNC25.

References

[1] Fatemi J, Lemmen MHJ. Effective Thermal/Mechanical Properties of Honeycomb Core Panels for Hot Structure Applications. Journal of Spacecraft and Rockets 2009;46:514-525.

[2] Wang D, Ye L, Lu Y, Li F. A damage diagnostic imaging algorithm based on the quantitative comparison of Lamb wave signals. Smart materials and structures 2010;19(6):065008.

[3] Rizov V, Shipsha A, Zenkert D. Indentation study of foam core sandwich composite panels. Composite structures. 2005 Jun 30;69(1):95-102.

[4] Shipsha A, Hallström S, Zenkert D. Failure mechanisms and modelling of impact damage in sandwich beams-a 2D approach: part I-experimental investigation. Journal of Sandwich Structures & Materials. 2003 Jan;5(1):7-31.

[5] Zenkert D. The handbook of sandwich construction. London, EMAS Publishing, 1997.

[6] Abrate S. Impact on composite structures. Cambridge university press; 2005 Aug 22.

[7] Kreculj D, Rasuo B. Review of impact damages modelling in laminated composite aircraft structures/Pregled modeliranja udarnih ostecenja u laminatnim kompozitnim konstrukcijama letjelica. Tehnicki Vjesnik-Technical Gazette. 2013 May 1;20(3):485-96.

[8] Davies GAO, Hitchings D, Ankersen J. Predicting Delamination and Debonding in Modern Aerospace Composite Structures. Composites Science and Technology 2006;66(6):846–854.

[9] Mikulik Z. Application of fracture mechanics to predict the growth of single and multi-level delaminations and disbonds in composite structures. School of Mechanical and Manufacturing Engineering, University of New South Wales, Sydney. 2008 Oct;308.

[10] Lamboul B, Passilly B, Roche JM, Osmont D. Impact damage detection in sandwich composite structures using Lamb waves and laser vibrometry. InAIP Conference Proceedings 2013 Jan 25 (Vol. 1511, No. 1, pp. 1003-1010). AIP.

[11] Polimeno U, Meo M, Almond DP, Angioni SL. Detecting low velocity impact damage in composite plate using nonlinear acoustic/ultrasound methods. Applied Composite Materials. 2010 Oct 1;17(5):481-8.

[12] Růžek R, Lohonka R, Jironč J. Ultrasonic C-Scan and shearography NDI techniques evaluation of impact defects identification. NDT & E International. 2006 Mar 31;39(2):132-42.

[13] Safri SN, Sultan MT, Jawaid M, Jayakrishna K. Impact behaviour of hybrid composites for structural applications: A review. Composites Part B: Engineering. 2017 Sep 14.

[14] Mustapha S, Ye L. Propagation behaviour of guided waves in tapered sandwich

structures and debonding identification using time reversal. Wave Motion. 2015 Sep 30;57:154-70.

[15] Pieczonka L, Ukowski P, Klepka A, Staszewski WJ, Uhl T, Aymerich F. Impact damage detection in light composite sandwich panels using piezo-based nonlinear vibro-acoustic modulations. Smart Materials and Structures. 2014 Sep 16;23(10):105021.

[16] Luchinsky DG, Hafiychuk V, Smelyanskiy VN, Kessler S, Walker J, Miller J, Watson M. Modeling wave propagation and scattering from impact damage for structural health monitoring of composite sandwich plates. Structural Health Monitoring. 2013 May;12(3):296-308.

[17] He F, Zhou Z, Feng Z. Research on an inspection method for de-bond defects in aluminum skin-honeycomb core sandwich structure with guided waves. In17th world conference on nondestructive testing 2008 Oct.

[18] Hay TR, Wei L, Rose JL, Hayashi T. Rapid inspection of composite skin honeycomb core structures with ultrasonic guided waves. Journal of Composite Materials. 2003 May;37(10):929-39.

[19] Lowe MJ, Challis RE, Chan CW. The transmission of Lamb waves across adhesively bonded lap joints. The Journal of the Acoustical Society of America. 2000 Mar;107(3):1333-45.

[20] Ostachowicz W, Kudela P, Krawczuk M, Zak A. Guided waves in structures for SHM: the time-domain spectral element method. John Wiley & Sons; 2011 Dec 30.

[21] Xu B, Giurgiutiu V. Single mode tuning effects on Lamb wave time reversal with piezoelectric wafer active sensors for structural health monitoring. Journal of Nondestructive Evaluation. 2007 Dec 1;26(2):123-34.

[22] Baid H, Schaal C, Samajder H, Mal A. Dispersion of Lamb waves in a honeycomb composite sandwich panel. Ultrasonics. 2015 Feb 28;56:409-16.

[23] Sikdar S, Banerjee S. Structural Health Monitoring of Advanced Composites Using Guided Waves. LAP LAMBERT Academic Publishing, 2017; ISBN 978-620-2-02697-0.

[24] Sen S, Bhattacharya B. Online structural damage identification technique using constrained dual extended Kalman filter. Structural Control and Health Monitoring. 2017 Sep 1;24(9).

[25] Kudela P, Radzieński M, Ostachowicz W. Identification of cracks in thin walled structures by means of wavenumber filtering. Mechanical Systems and Signal

Processing. 2015 Jan 31;50:456-66.

[26] Ruzzene M, Jeong SM, Michaels TE, Michaels JE, Mi B. Simulation and measurement of ultrasonic waves in elastic plates using laser vibrometry. InAIP Conference Proceedings 2005 Apr 9 (Vol. 760, No. 1, pp. 172-179).AIP.

[27] Michaels TE, Michaels JE, Ruzzene M. Frequency–wavenumber domain analysis of guided wavefields. Ultrasonics. 2011 May 31;51(4):452-66.

[28] Staszewski WJ, Lee BC, Mallet L, Scarpa F. Structural health monitoring using scanning laser vibrometry: I. Lamb wave sensing. Smart Materials and Structures. 2004 Feb 4;13(2):251.

[29] Kudela P, Radzienski M, Ostachowicz W. Damage visualization enhancement by the wave field filtering and processing. InSPIE Smart Structures and Materials+ Nondestructive Evaluation and Health Monitoring 2012 Apr 26 (pp. 83471H-83471H). International Society for Optics and Photonics.

[30] Sohn H, Dutta D, Yang JY, Desimio MP, Olson SE, Swenson ED. A wavefield imaging technique for delamination detection in composite structures. Korea Advanced Inst of Science and Technology Daejeon (Korea); 2010 Aug.

[31] Qiao P, Yang M. Impact analysis of fiber reinforced polymer honeycomb composite sandwich beams. Composites Part B: Engineering. 2007 Sep 30;38(5):739-50.

[32] Backstöm D, Nilsson A. Modeling flexural vibration of a sandwich beam using modified fourth-order theory. Journal of Sandwich Structures & Materials. 2006 Nov;8(6):465-76.

[33] Sorokin SV. Analysis of propagation of waves of purely shear deformation in a sandwich plate. Journal of sound and vibration. 2006 Apr 4;291(3):1208-20.

[34] Nosier A, Kapania RK, Reddy JN. Free vibration analysis of laminated plate using a layerwise theory. AIAA Journal. 1993:31:2335-46.

[35] Hay TR, Wei L, Rose JL, Hayashi T. Rapid inspection of composite skin honeycomb core structures with ultrasonic guided waves. Journal of Composite Materials. 2003 May;37(10):929-39.

[36] Castaings M, Hosten B. Guided waves propagating in sandwich structures made of anisotropic, viscoelastic, composite materials. The Journal of the Acoustical Society of America. 2003 May;113(5):2622-34.

[37] Liu L, Bhattacharya K. Wave propagation in a sandwich structure. International Journal of Solids and Structures. 2009 Aug 15;46(17):3290-300.

[38] Banerjee S, Pol CB. Theoretical modeling of guided wave propagation in a sandwich

plate subjected to transient surface excitations. International Journal of Solids and Structures. 2012 Nov 15;49(23):3233-41.

[39] Soorgee MH, Lissenden CJ, Rose JL, Yousefi-Koma A. Planar guided waves for SHM of plate structures using piezoelectric fiber transducers. InAIP Conference Proceedings 2013 Jan 25 (Vol. 1511, No. 1, pp. 254-261). AIP.

[40] Zhao X, Gao H, Zhang G, Ayhan B, Yan F, Kwan C, Rose JL. Active health monitoring of an aircraft wing with embedded piezoelectric sensor/actuator network:I. Defect detection, localization and growth monitoring. Smart materials and structures. 2007 Jun 29;16(4):1208.